Journal of Materials Chemistry C

ROYAL SOCIETY OF CHEMISTRY

PAPER

View Article Online
View Journal | View Issue

Cite this: J. Mater. Chem. C, 2025, 13, 20589

A solvent crafted alternate [Zn_3/Zn_4] cluster driven MOF and its analogous MOG: structural elucidation integrated with advanced bilirubin detection and encryption strategies

Joydeep Ray,[a] Sumit Mondal,[a] Pallav Mondal[b] and Debajit Sarma *[a]

Received 2nd April 2025,
Accepted 26th August 2025

DOI: 10.1039/d5tc01391g

rsc.li/materials-c

The synergy between coordination chemistry and materials design facilitates the development of sophisticated luminescent systems with advanced applications. This study details the preparation and analysis of a rare alternate [Zn_3/Zn_4] cluster-based metal–organic framework (MOF), **SSICG15**, and its analogous metal–organic gel (MOG), **SSICG15-MOG**, both originating from the same naphthalimide ligand (H_2L) and zinc precursor. The existence of trinuclear and tetranuclear zinc clusters, distinctive to the structure, offers substantial insights into the coordinating environment of the MOF structure. The xerogel, obtained from the MOG, exhibited notable crystallinity as evidenced by PXRD studies. The probable structure of the MOG was determined by simulating the PXRD data of the related xerogel using molecular dynamics simulations, informed by ESI-MS data and the coordination network of the MOF. Both materials exhibited exceptional luminescence, facilitating their application in sophisticated anticounterfeiting methods, including QR code encoding along with anticounterfeiting ink preparation. These materials show great sensitivity and selectivity for the detection of bilirubin (BR), which is a crucial biomarker for jaundice diagnosis and monitoring, with a LOD of 20 nM for **SSICG15-MOG** and 26.5 nM for **SSICG15**. Both materials combine photonic capabilities with excellent diagnostic accuracy, which makes them extremely attractive for analytical and biological applications.

1. Introduction

The development of multifunctional inorganic hybrid materials has gained prominence as a highly valuable category of materials owing to their capacity to integrate the beneficial characteristics of inorganic constituents with the adaptability of organic molecules.[1–5] This process of hybridization enables the creation of materials with customized capabilities, rendering them appropriate for a diverse array of applications, such as catalysis,[6–11] sensing,[12–16] energy storage,[17,18] drug delivery,[19–21] and information encryption.[22,23] Metal–organic frameworks (MOFs) exemplify this domain, providing a distinctive blend of structural adaptability and functional diversity. Metal–organic frameworks (MOFs) exhibit highly ordered crystalline structures created through the coordination of metal ions or clusters with organic linkers, yielding materials with remarkably large surface areas and porosity. These structural characteristics endow MOFs with exceptional capability for gas storage,[24] separation,[25] catalysis,[26] and sensing applications.[27] The crystalline structure of MOFs enables meticulous regulation of pore dimensions, functionality, and the chemical environment, which can be optimized *via* systematic design and post-synthetic modification techniques.[28] Their modular architecture facilitates the integration of various metal centers and organic ligands, rendering MOFs highly adaptable platforms for specific applications.

The discipline of MOFs was established by the pioneering work of Yaghi and co-workers, who first conceptualized and developed this excellent class of materials.[29,30] Metal–organic frameworks (MOFs) have been established as key hybrid materials, while recent developments have introduced metal–organic gels (MOGs) as an equally promising class within this field.[31,32] The insertion of metal components into a gel matrix is a very efficient method for the development of soft materials that possess desirable attributes such as optical properties, magnetic responsivity, self-healing activity, catalytic efficiency, and many more.[33–36] Steed and co-workers' work has significantly enhanced this creative approach to developing materials and has played a key role in the establishment of the discipline of MOGs.[37,38] While fundamentally different in their structural organization, one is a soft, dynamic network and the other is a

[a] Department of Chemistry, Indian Institute of Technology Patna, Bihar 801106, India. E-mail: debajit@iitp.ac.in
[b] Department of Chemistry, National Institute of Technology Durgapur, West Bengal 716209, India

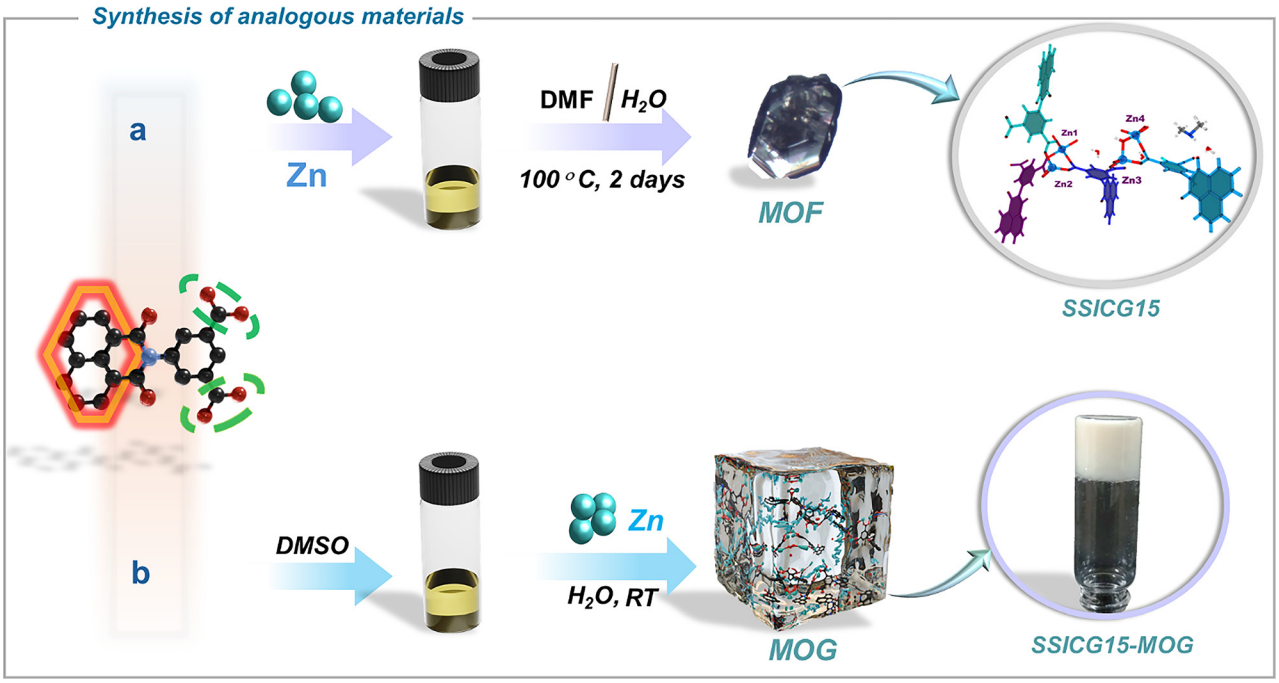

Scheme 1 Schematic illustration of the synthesis of the MOF/MOG: (a) highly ordered structure and (b) the sequential self-assembly.

rigid, crystalline framework, both the MOG and MOF are rooted in the same metal–ligand coordination chemistry.[39,40] It is essential to emphasize that MOFs have been extensively studied for applications benefiting from their strong crystallinity and well-defined porosity. Their accessible metal sites enable remarkable catalytic activity and selectivity, while their ability to selectively adsorb target analytes allows for highly efficient sensing.[41,42] This heterogeneity in structure has a direct impact on the advantages and drawbacks that are associated with MOFs and MOGs. Due to its well-defined structure, MOF functionalization may be accurately regulated *via* targeted synthetic techniques, allowing for the fine-tuning of functionalities.[43] Nonetheless, the large-scale production of MOFs continues to be a formidable and unresolved challenge.

Conversely, MOGs generally display a less distinct structural identity owing to their frequent colloidal characteristics. Nonetheless, their simple synthesis and ability for large-scale production – exhibiting features akin to those of MOFs – render MOGs a compelling platform for further investigation. This close association underscores the broader concept of analogous materials, wherein minor alterations in synthetic circumstances, such as solvent selection or the reaction environment, can result in the emergence of structurally diverse yet compositionally comparable materials. Dastidar and co-workers have implemented this concept by synthesizing MOGs and their analogous coordination polymers from the same mix of metal cations and binding ligands.[44] The concept of structural variety within a fundamental compositional framework is especially important when investigating the structural properties of MOGs. Combining experimental methods with molecular dynamics (MD) simulations allows one to achieve structural precision in MOGs by thoroughly knowing their static and dynamic features.[45] The intrinsically dynamic characteristics of MOGs, especially their capacity to react to external stimuli and environmental fluctuations, pose challenges for comprehensive understanding through static experimental techniques alone. In this regard, MD simulations seem to be extremely useful.[46]

The act of counterfeiting and duplicating security documents, such as currency, passports, banknotes, credentials, and licenses, is a recurring problem that poses a significant worldwide issue. This illicit activity results in substantial financial losses up to billions of dollars for corporations, governments, and customers.[47–50] In recent years, luminescent materials made up of lanthanide metal ions have been a choice of interest as sensing probes and anticounterfeiting materials for their interesting characteristics as luminescent materials like highly characterized emission in the visible region, elevated quantum yields, and long lifespans.[51] However, the costs associated with producing lanthanide materials are not economically feasible due to the inclusion of rare earth elements. A notable drawback of employing lanthanides is their diminished luminosity, attributable to the quenching effects of the solvent and the self-quenching of the prolonged excited state.[52] There is a pressing demand for cost-effective, easily produced materials that provide long-lasting luminescent properties with a wide range of potential applications.

The critical requirement for advanced materials is not only restricted to anticounterfeiting, but it also applies to healthcare, where precise identification is highly essential. From the clinical significance of bilirubin (BR), there is considerable

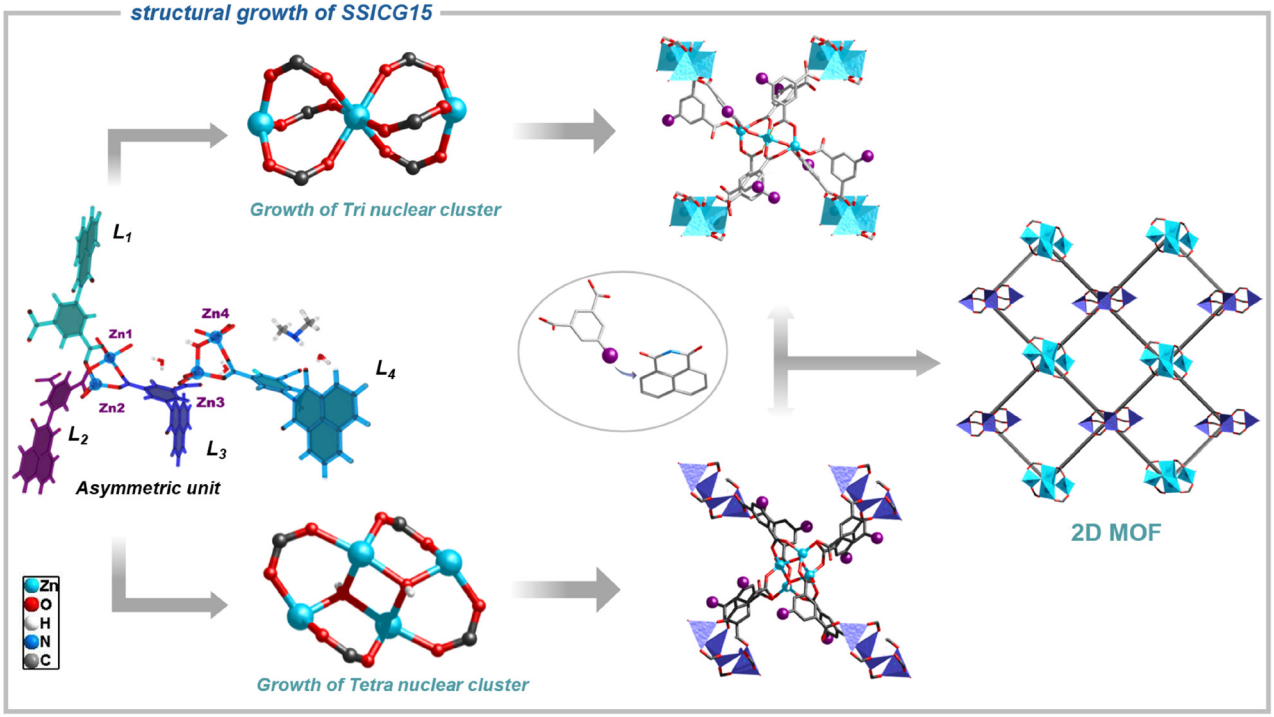

Scheme 2 Schematic representation of the formation of the [Zn_3/Zn_4] cluster-driven MOF.

interest in detecting BR to diagnose jaundice. An excessive concentration of unbound BR is very detrimental to the human body since it can traverse the blood–brain membrane and gather in the brain, resulting in cerebral hemorrhage.[53] Excess unbound BR can lead to mental health difficulties, hepatitis, and even death. BR levels typically range from 1.2 to 2.95 mg dL^{-1}, rarely reaching 5 mg dL^{-1}, but can reach 20 mg dL^{-1} in adults and 50 mg dL^{-1} in extreme cases.[54,55] The BR level is measured using the diazo or peroxidase techniques, which detect color changes in serum. However, the diazo technique can produce false positives by detecting amines, is pH-dependent, and necessitates sample preparation to separate proteins that frequently co-precipitate with BR.[56] In comparison to those methods, fluorometric procedures are advantageous in detecting free BR due to their high specificity and sensitivity. Additionally, they are convenient for preparing samples and may operate effectively across a wide range of concentrations.[57] In recent years, there have been a limited number of composite materials documented for the detection of BR. In a recent publication, Lu *et al.* have developed a fibrous device based on bimetallic MOFs for non-invasive BR sensing.[58] Nandi *et al.* have post-synthetically modified an Al(III) based MOF for the detection of BR in human biofluids.[59] In the absence of previous research on the utilization of MOGs for bilirubin detection, their inherent adaptability and ability to engage in specific metal–analyte interactions underscore their promise as innovative materials for prospective applications.

Herein, we have synthesized a Zn-mediated MOG and MOF with slight variations in their synthetic procedures to serve the purpose of crafting analogous materials (Scheme 1). The multifunctional naphthalimide core-based dicarboxylic ligand has been utilized to facilitate the formation of the materials. The construction of coordination-driven frameworks or self-assembled structures significantly improves luminescent characteristics by amplifying emission. Although the Zn cluster core contributes minimally to this development, the augmented stiffness of the framework is crucial. This stiffness of the metal–ligand framework constrains molecular vibrations and rotations that usually facilitate non-radiative decay processes. By inhibiting these processes, the framework diminishes energy dissipation and markedly enhances fluorescence intensity.[60] Furthermore, to comprehend the structural and dynamic characteristics, a molecular dynamics study was conducted utilizing the experimental data of both the MOF and the as-synthesized MOG. This computational method allowed us to examine the atomic and molecular interactions within the gel over time, yielding insights into the material's structural flexibility and responsiveness. The reliable photoluminescent response and sol–gel transformability of the MOG as an anticounterfeiting QR code have facilitated in the creation of a secure and functional encryption material. Fabrication of security inks with both **SICG15-MOG** and **SSICG15** significantly broadens their potential for extensive applications and opens new avenues for the development of secure optical tags. Furthermore, both the MOG and MOF have been studied as smart sensory probes for the detection of bilirubin (BR). The detection capability of both materials remains similar. The high K_{SV} of 1.98×10^5 M^{-1} for **SSICG15-MOG** and 4.7×10^4 M^{-1} of the SSICG15, along with low detection limits (20 nM and 25.6 nM) for BR, indicates excellent detection efficiency towards the analyte, making it an efficient sensory probe.

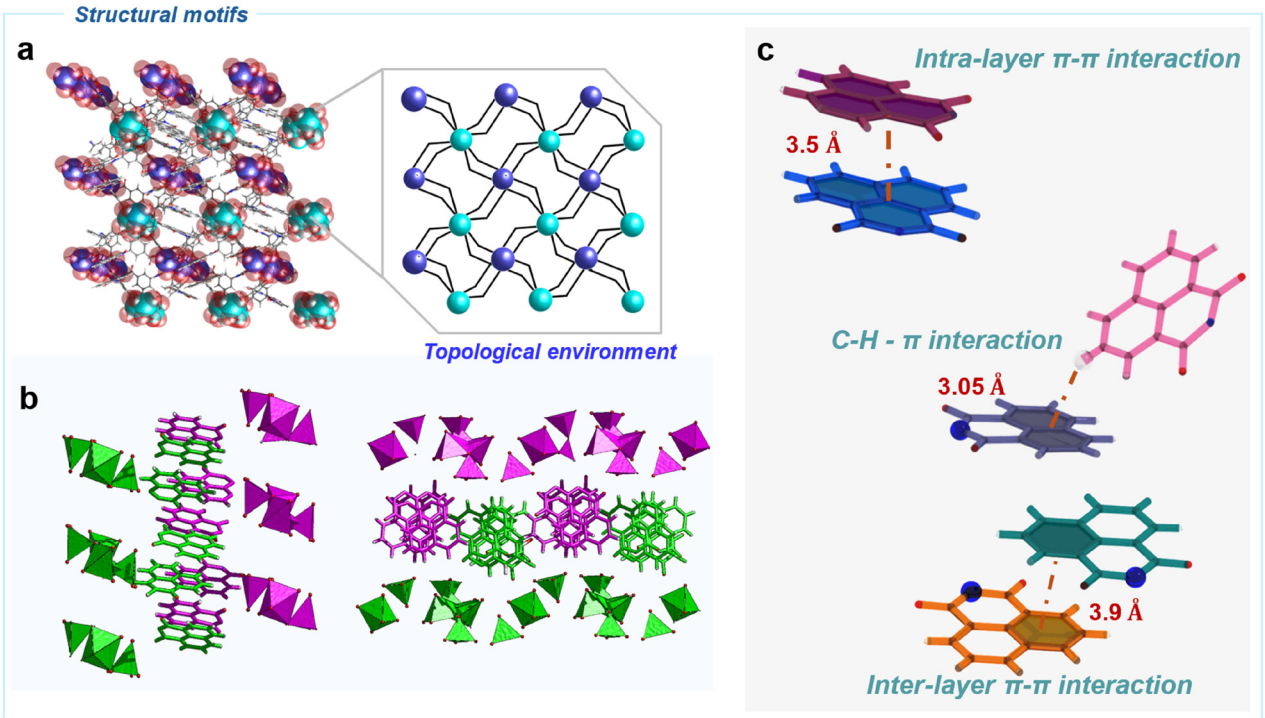

Fig. 1 (a) Simplified representation of **SSSICG15**. (b) Formation of a 3D structure through π–π stacking between two different 2D layers along the *a*- and *b*-axis. (c) Illustration of three distinct kinds of π–π stacking involved in the formation of the MOF.

2. Experimental section

2.1. Synthesis of SSICG15-MOG

A di-carboxylic acid-derived low molecular weight gelator (H_2L) incorporating a naphthalimide scaffold was employed for the synthesis of the metal–organic gel (MOG), in which zinc serves as the central metal node (Fig. S1, SI). The linker and nitrate salt of zinc were combined in a stoichiometric ratio of 1 : 1 to produce the MOG. A 0.1 M solution of $Zn(NO_3)_2{\cdot}6H_2O$ was prepared using water as a solvent. In a separate glass container, 1 mL of a 0.1 M solution of the linker was formulated using dimethyl sulfoxide (DMSO) as the solvent. Subsequently, the two distinct solutions were blended in an equivalent volume ratio within a 20 mL glass container, leading to the formation of a stable gel at ambient temperature (RT).

2.2. Synthesis of SSICG15

Homogeneous mixing of the linker H_2L (7.2 mg, 0.02 mmol) and $Zn(NO_3)_2{\cdot}6H_2O$ (5.94 mg, 0.02 mmol) was introduced into a solution of DMF/H_2O (1 : 1 v/v, 4 mL) within a reaction vial and securely sealed. The resulting mixture was heated in an oven at 100 °C for two days. The formation of off-white block-shaped crystals was observed. Finally, crystals were subsequently rinsed multiple times using a solution of acetone/H_2O.

3. Results and discussion

3.1. Structural study of SSICG15

The single crystal X-ray diffraction analysis demonstrated that **SSICG15** crystallized in a triclinic symmetry with the space group $P\bar{1}$. The asymmetric unit is made up of tetranuclear Zn(II) ions coordinated with four different H_2L ligands to form a 2D framework where Zn(1) is located at a spatial position with a 50% occupancy, whereas Zn(2), Zn(3) and Zn(4) are located at the interstitial position in the lattice with a 100% occupancy. A distinct coordination environment was observed where Zn(1) is coordinated with six oxygen atoms, Zn(2) and Zn(3) are both coordinated with four oxygen atoms and Zn(4) is coordinated with five oxygen atoms, respectively (Fig. S2, SI). Four distinct kinds of ligand conformations have been observed in the asymmetric unit, where L_1 and L_2 maintain the coordination of μ^2-$\eta^1\eta^1$ with Zn(1) and Zn(2). On the other hand, L_4 maintains a coordination of μ^2-$\eta^1\eta^1$ with Zn(3) and Zn(4). Distinctively, L_3 has established a bridging environment of μ^3-$\eta^1\eta^1$:$\eta^1\eta^0$. Zn(3) and Zn(4) have also been bridged by a μ^2-OH. The framework has been established through alternating connections between a tetranuclear Zn–O cluster and a trinuclear Zn–O cluster, where Zn(1) and Zn(2) form a trinuclear cluster and Zn(3) and Zn(4) form a tetranuclear cluster (Scheme 2). Four trinuclear clusters have surrounded the tetranuclear clusters through eight coordinating ligands, while the trinuclear clusters have also been surrounded by four tetranuclear clusters through eight coordinating ligands. (Fig. 1a and Fig. S3, SI). The stabilization of the framework was established by the engagement of naphthalimide rings in distinct π–π interactions. The 2D covalent sheets participate in π–π interactions with neighbouring sheets on both sides, resulting in the formation of a 3D SMOF (supramolecular metal–organic framework) (Fig. 1b and Fig. S4, SI). Interactions involving π electrons occur between the naphthalimide rings of neighbouring sheets within a distance of 3.9 Å, while interactions involving π electrons

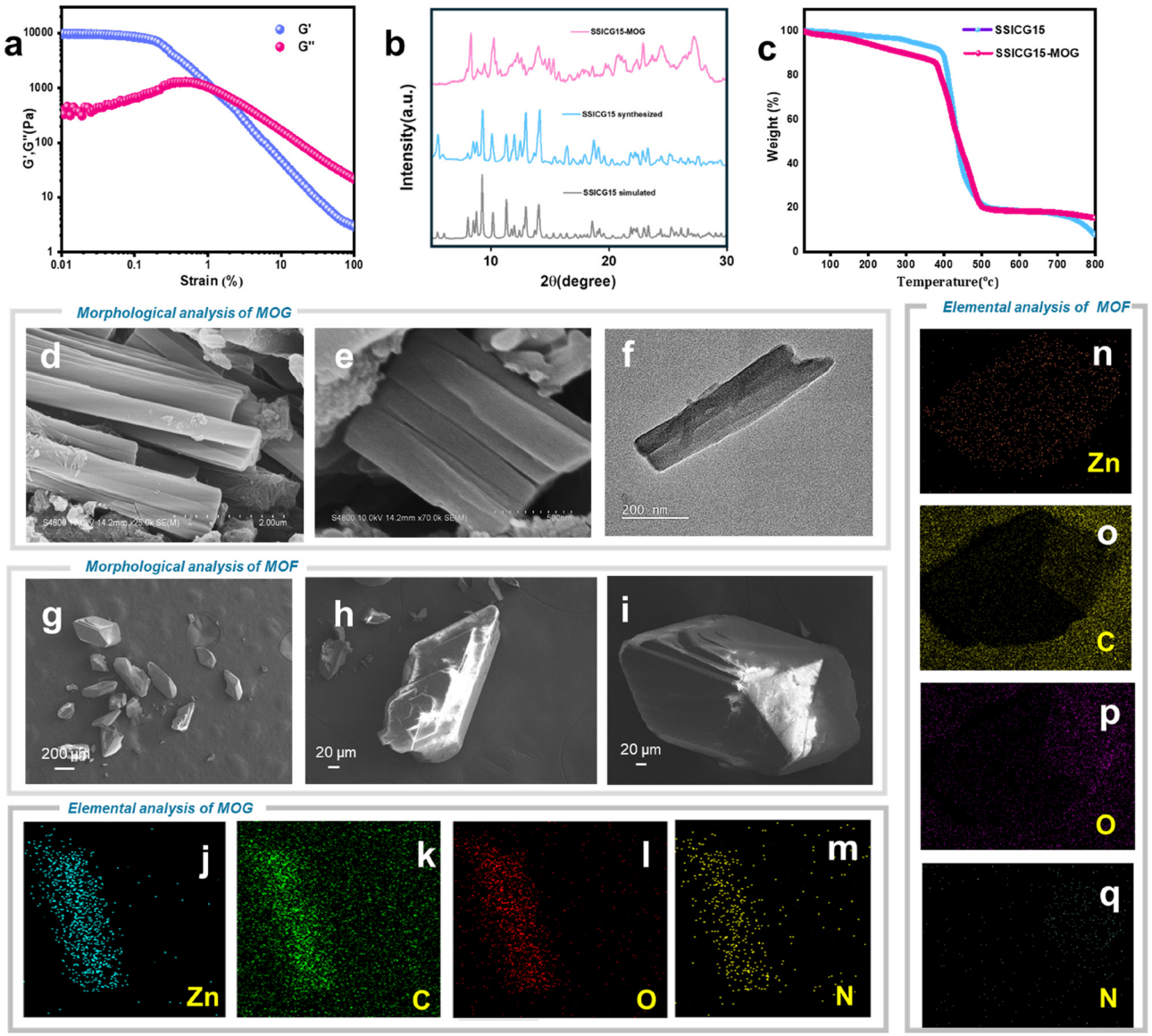

Fig. 2 (a) Amplitude sweep graph for **SSICG15-MOG;** (b) PXRD patterns of **SSICG15** and **SSICG15-MOG**; (c) TGA curves of **SSICG15** and **SSICG15-MOG;** (d) and (e) FESEM images of **SSICG15-MOG;** (f) TEM image of **SSICG15-MOG;** (g)–(i) FESEM images of **SSICG15;** (j)–(m) elemental analysis of **SSICG15-MOG;** and (n)–(q) elemental analysis of **SSICG15**.

within the same sheet occur within a distance of 3.5 Å and a distance of 3.05 Å for CH–π interactions (Fig. 1c)

3.2. Gelation and characterization

The highly fluorescent MOG was synthesized by mixing the gelator (H_2L) with zinc nitrate in a DMSO/H_2O medium at room temperature. Instant gelation occurred upon combining an equimolar (1 : 1) solution of H_2L in DMSO with an aqueous solution of zinc nitrate (Scheme 1). Solubility parameters were checked for the gelator in different solvents, but the gelator (H_2L) solubilized only in DMSO (Table S2, SI). So further experiments were carried out using DMSO as the solvent medium. The extent of gelation was evaluated at varying concentrations of the gelator and metal ions. Significant gelation was observed only in 0.1 M solutions in a 1 : 1 molar ratio (Table S3, SI). An organogel was reported in earlier studies using a ratio of H_2L in DMSO and water; however, little or no luminescence was observed.[61] The selection of linkers is essential for efficient gelation. The utilization of H_2L as a gelator is advantageous owing to its carboxylate functionality, which facilitates the coordination with zinc, whereas the imide group and strongly conjugated aromatic moieties promote self-assembly *via* supramolecular contacts (N & C=O) and robust π–π interactions among aromatic rings. To verify the gelation ability of the freshly prepared **SSICG15-MOG**, the viscoelastic properties were analysed alongside the ''inversion test'' (Scheme 1).

The amplitude sweep study was performed at a constant angular frequency (ω) of 10 rad s^{-1}, with shear strain values ranging from 0.01% to 100%. At low strain values, although the

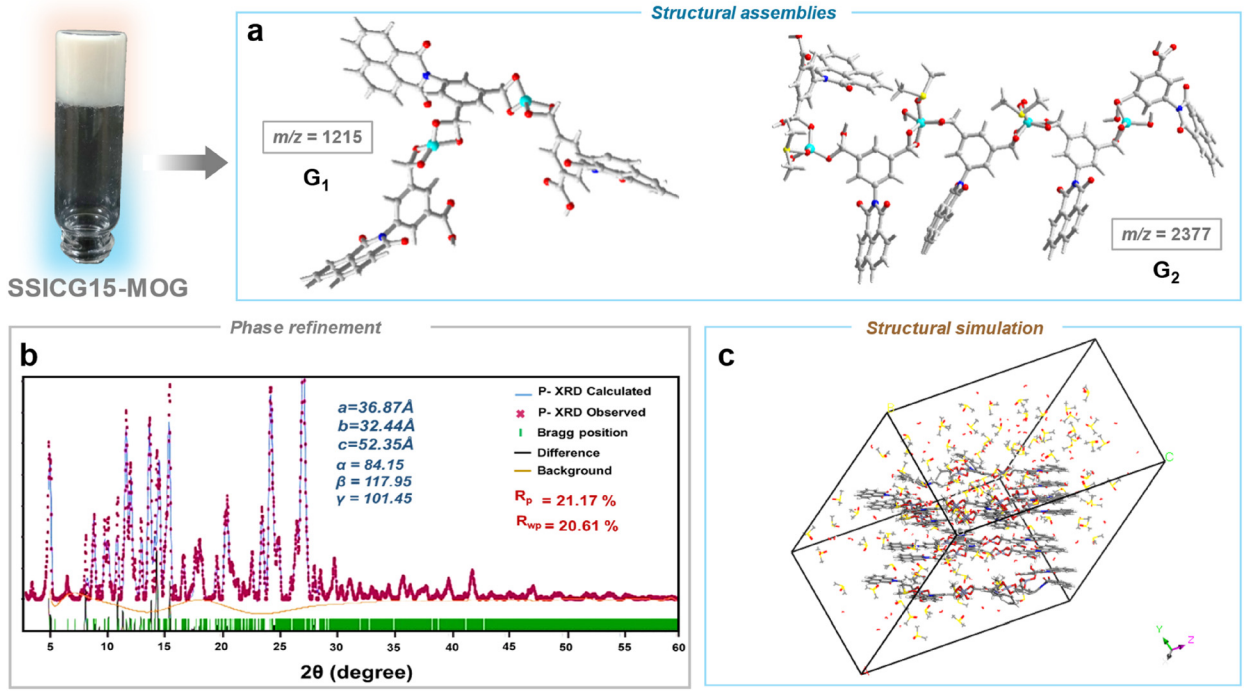

Fig. 3 (a) Structural assemblies of the identified assembly G1 and G2 at m/z = 1215 and 2377; (b) Rietveld refinement of the PXRD pattern of as-synthesized **SSICG15-MOG;** and (c) molecular dynamics simulation of the stacked assembly in the presence of the DMSO/H_2O solvent.

applied strain was insufficient to disrupt the network, the storage modulus (G') remained higher than the loss modulus (G''), indicating a stable gel state. As the strain increased beyond a certain threshold, the loss modulus surpassed the storage modulus, marking the transition from a gel state to a sol state, commonly referred to as the cross-over point.

The yield strain corresponding to this transition was determined to be 1.2% (Fig. 2a). Furthermore, the viscoelastic properties of the gel were investigated using a frequency sweep experiment. The experiment was conducted within the frequency range of 100 radians per second to 1 radian per second. No correlation was detected between G' and G'' across all frequencies. The curve exhibits the concurrent behaviour of the storage and loss moduli, indicating the robustness of the gel phase with its viscoelastic properties (Fig. S5, SI). Additionally, to further investigate the MOG's integrity, an ESI-MS analysis was conducted. Distinct peaks were observed at m/z = 1215 and 2377, which can be attributed to the coordination between the metal, ligand, and solvent molecules (Fig. S6–S8, SI). For the as-synthesized xerogel and MOF, powder X-ray diffraction (PXRD) was performed to check the crystallinity and phase purity. A sharp intense diffraction pattern was observed, which signifies the long-range ordered structural integrity of the xerogel. The PXRD patterns of **SSICG15** were analysed and compared with the simulated pattern of the MOF, confirming the phase purity of the material (Fig. 2b). Thermogravimetric analysis (TGA) was performed to evaluate the stability of both materials over the temperature range from room temperature (RT) to 800 °C. The **SSICG15-MOG** sample exhibited a gradual weight loss of approximately 7–9 wt%, which can be attributed to the release of trapped solvent molecules and physisorbed moisture. The nearly similar TGA profiles of **SSICG15-MOG** and **SSICG15** imply a comparable underlying framework and thermal stability up to 400 °C, signifying a stable framework of the MOF and MOG with a uniform coordinating environment in both. Beyond this point, a significant decrease in weight percentage was observed, indicating the disintegration of the framework (Fig. 2c). To assess the morphological characteristics of the synthesized materials, both **SSICG15-MOG** and its corresponding crystalline MOF, **SSICG15**, were examined using scanning electron microscopy (SEM) and high-resolution transmission electron microscopy (HRTEM). For **SSICG15-MOG**, SEM images revealed a stacked rod-like fibrous morphology (~1–2 μm), which was further corroborated by HRTEM, showing rod-like structures in the range of 20–200 nm (Fig. 2d–f). Energy-dispersive X-ray spectroscopy (EDX) and elemental dot mapping analyses confirmed the homogeneous distribution of all constituent elements within **SSICG15-MOG** (Fig. 2j–m). In contrast, the parent crystalline MOF **SSICG15**, synthesized under analogous conditions but without gelator-assisted assembly, exhibited a well-defined block-shaped morphology in SEM images, indicative of the formation of uniform crystalline domains (Fig. 2g–i). EDX and elemental mapping of **SSICG15** also demonstrated an even spatial distribution of all elements (Fig. 2n–q). The surface area of **SSICG15-MOG** and **SSICG15** was ascertained using N_2 adsorption–desorption experiments at 77 K. The BET surface areas were measured at 13 $m^2\ g^{-1}$ for **SSICG15-MOG** and 11 $m^2\ g^{-1}$ for **SSICG15**. The analysis of pore size distribution indicated average pore diameters of 2.12 nm for **SSICG15-MOG** and 2.20 nm for **SSICG15**, implying a minor shrinkage of the

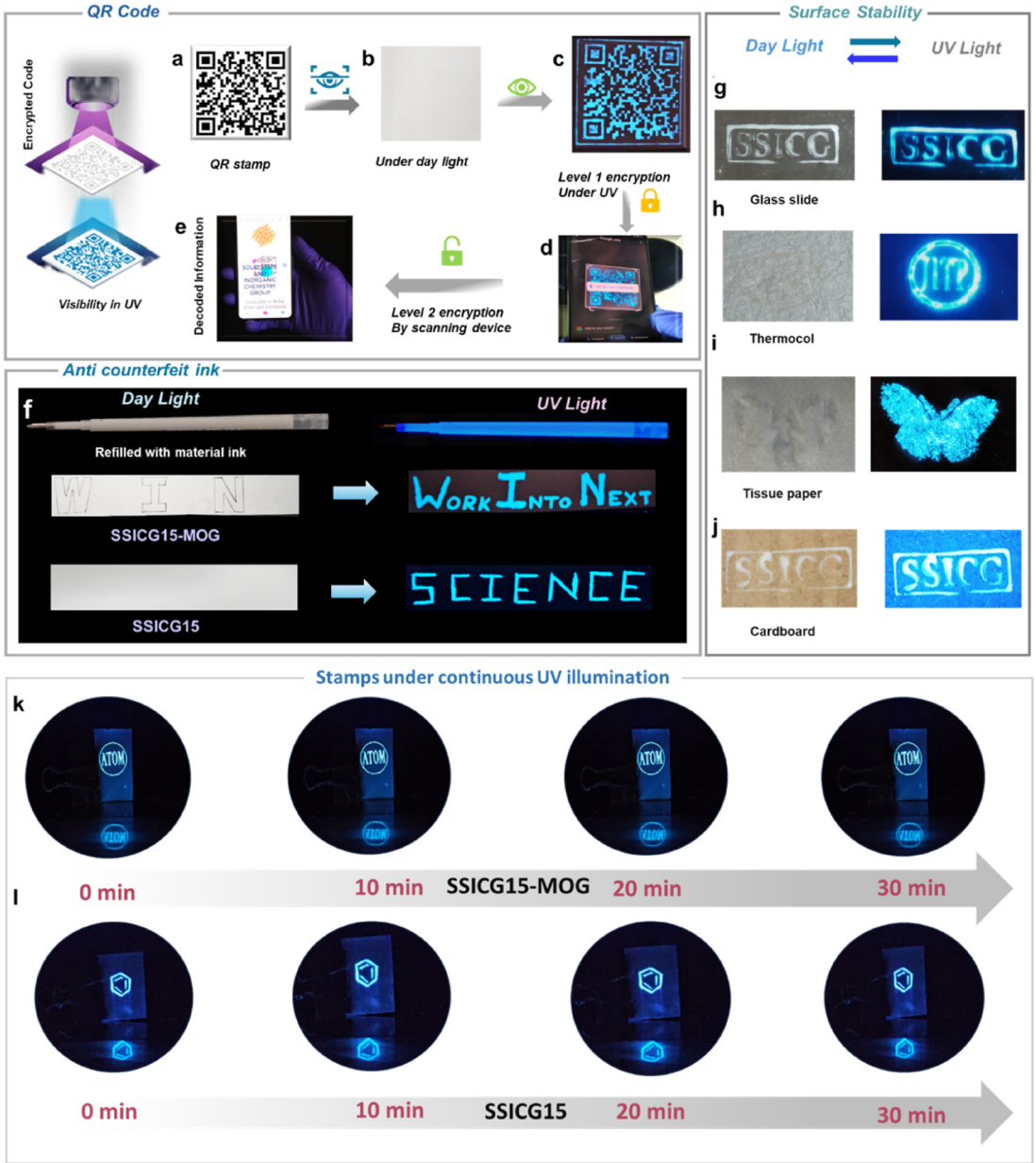

Fig. 4 (a) Image of the raw QR code; (b) stamped QR code in daylight; (c) visibility of the QR code in the presence of UV light; (d) image of the encrypted code while scanning with an electronic device; (e) image of decoded encrypted information; (f) image of the coded phrase (WORK INTO NEXT) with **SSICG15-MOG** and (SCIENCE) with **SSICG15** using anticounterfeiting ink in the absence and presence of UV light; (g)–(j) anticounterfeiting stampings on different surfaces: (g) glass slide, (h) thermocol, (i) tissue paper, and (j) cardboard; (k) and (l) stability of **SSICG15-MOG** and **SSICG15** in stamping under continuous UV irradiation.

pore structure during MOG production (Fig. S9 and S10). The stability tests were conducted on **SSICG15-MOG** and **SSICG15** by subjecting them to diverse solvent environments, including DMF, acetonitrile, methanol, and water, as well as varying the pH (pH 3 and pH 10). Powder X-ray diffraction (PXRD) analysis was conducted to assess the structural integrity of both materials post-treatment.

The findings demonstrated that both **SSICG15-MOG** and **SSICG15** exhibited robust structural stability in the majority of solvents evaluated. A minor structural disturbance was observed under acidic conditions (pH = 3), indicating a degree of vulnerability of the materials to highly acidic environments (Fig. S30 and S31).

3.3. Probable structure and energy profiling of SSICG15-MOG

The probable structure of the MOG (**SSICG15-MOG**) was simulated by molecular dynamics simulations based on the ESI-MS data and the powder X-ray diffraction pattern of the xerogel. The PXRD pattern obtained for the xerogel consists of sharp peaks indicating crystallinity and long-range order, which are

comparable to those of the MOF. The gel phase, as determined from the ESI-MS analysis, consists of two major assemblies with molecular weights of 1215 u (G1) and 2377 u (G2) (Fig. S6–S8, SI). The coordination environment around the metal ions was interpreted based on the crystal structure of the MOF and correlated with the mass spectrometry data. Assembly G1 comprises five ligand units coordinated to four Zn(II) ions, along with three DMSO molecules and a water molecule, whereas assembly G2 contains three ligand units coordinated to two Zn(II) ions (Fig. 3a). The structural properties and intermolecular packing of the MOG between the two were examined. Further intermolecular packing models were simulated to reveal its packing model along with the solvents. To simplify the system, other low-intensity assemblies were neglected from the mass data. As the MOG has well-diffracted powder data, the unit cell parameters and the long-distance packing were analysed through PXRD. Based on the experimental powder XRD pattern, the xerogel was indexed to a unit cell with parameters a = 36.87 Å, b = 32.44 Å, and c = 52.35 Å, and angles $\alpha = 84.15^\circ$, $\beta = 117.95^\circ$, and $\gamma = 101.45^\circ$. The Rietveld refinement yielded an R_{wp} value of 20.61%, indicating a reasonably good fit for a metallogel. This value, however, is slightly higher compared to typical solid-state materials, which can be attributed to ongoing solvent interactions and the presence of mixed fragments, as suggested by the mass spectrometry data (Fig. 3b). Notably, the crystal plane (111), corresponding to 5.13° for a d-spacing of 17.2 Å, was used as the basis for stacking assembly in the MOG.[62] The simulation of the stacking of assemblies G1 and G2 was conducted.[63] The stacking pattern demonstrates the influence of DMSO/H_2O solvent molecules, which are crucial for maintaining the gel in the sol phase, as indicated by molecular dynamics simulations. The bimolecular stacking energy is approximately 3.59 kcal mol^{-1}, and solvent contact reduces the system's energy by about 8.2 kcal mol^{-1}.[64] This indicates that the interaction energy was further decreased due to solvent interactions and makes the system more stable (Fig. 3c).[65,66]

3.4. Photophysical study

The photophysical characteristics of the as-synthesized MOF and xerogel were studied. Both materials emit in the blue region with a wavelength of 485 nm when excited at 385 nm (Fig. S11, SI). The photoluminescence spectroscopy data in the chromaticity diagram (CIE 1931) refer to (0.31,0.19) coordinates for **SSICG15-MOG** and (0.16, 0.24) for **SSICG15**, which confirmed the blue emission (Fig. S12 and S13, SI).[67] To obtain a thorough understanding of the MOG's photophysical characteristics, the quantum yields were examined. The quantum yield of **SSICG15-MOG** was determined to be 0.1 (eqn (S1), SI). The fluorescence intensity of the xerogel was analyzed across a spectrum of solvents, from very polar to non-polar, including water, methanol, ethanol, DMF, THF, chloroform, toluene, hexane, and diethyl ether (Fig. S14). The data unequivocally demonstrate that solvent polarity significantly affects emission behavior, with water displaying the highest fluorescence intensity peak and diethyl ether the lowest. This phenomenon can be ascribed to variations in the dielectric constants of the solvents, wherein highly polar solvents with elevated dielectric constants augment the stabilization of excited states, consequently enhancing emission intensity, while non-polar solvents with diminished dielectric constants offer negligible stabilization, leading to less fluorescence. Subsequent sensing experiments were conducted in an aqueous medium.[68,69]

To evaluate the photophysical efficiency of the material, solid and solution phase luminescent data were collected for the discrete ligand and synthesized material, which showed an increase in fluorescence intensity after the formation of the material (Fig. S15–S17). A leaching test was performed to evaluate the stability and no fluorescence intensity was observed with the filtrate of the xerogel from the aqueous medium (Fig. S18, SI). The Zn-based MOG and MOF demonstrate remarkable optical properties, emitting blue luminescence when exposed to UV light at a wavelength of 365 nm. The photoluminescent characteristics underscore the potential of these materials as efficient anti-counterfeiting agents, offering a distinctive and visible marker for security applications. The colloidal-state MOG, which can be easily manufactured in a single step, was chosen for additional studies due to its promising applications as a sensory probe and a direct predecessor to encryption applications.

3.5. Anticounterfeiting and encryption strategy

The highly luminescent material **SSICG15-MOG** was effectively established as a durable anticounterfeiting agent *via* the creation of a UV-responsive QR code (Fig. 4a). The QR code, imprinted with the luminescent material, is imperceptible in ambient daylight but becomes visible under 365 nm UV light, facilitating secure authentication and subsequent scanning with conventional QR code readers (Fig. 4b and c). A 4 cm × 4 cm non-fluorescent white template was used for its strong contrast and reliable visibility under many lighting conditions, as well as a non-reflective background that enhances scanning precision and security, rendering the QR code an optimal medium for encrypted information transmission. Furthermore, an encryption ink developed with the MOG was used to inscribe the words "WORK INTO NEXT", which is discernible solely under UV light, but under daylight, only the word "WIN" is visible. Similarly, an ink-based demonstration was carried out using **SSICG15**, wherein the word "SCIENCE" was inscribed. The resulting pattern exhibited optical characteristics comparable to those observed for the **SSICG15-MOG**-based ink, demonstrating their capacity for concealed communication and secure documentation (Fig. 4f). Additionally, the material's adhesion and stability were methodically assessed by producing luminescent stamps on multiple substrates, validating its adaptability and durability across different surfaces ranging from foam and tissue paper to sleek surfaces like Petri dishes and glass slides (Fig. 4g–j). A solvent stability test was conducted by dipping the luminescent stamp in a DMF solution for a defined time interval under continuous illumination to monitor any real-time fluorescence quenching. The stamp exhibited excellent stability with

negligible quenching in DMF (Fig. S20, SI). To maintain scientific rigor, similar tests were performed using various other solvents, including THF, hexane, water, methanol, toluene, and ethyl acetate, by drop-casting them onto the stamps (Table S4, SI). These results collectively demonstrate the robust luminescence stability of the material across diverse chemical environments. The words "**SSICG**" and "**IITP**" were observed pre- and post-exposure to different harsh environmental conditions, such as exposure to sunlight for continuous 2 days interval, high temperature at 200 °C overnight, immersion in liquid nitrogen, deep freezing conditions (−8 °C to −10 °C) for 2 days, and different acidic and basic pH conditions like (pH = 3, 7, 10), to check the durability of the material as a stamping template. It was noted that only in the case of pH = 3 a little quenching of fluorescence was observed, and no alteration of emission characteristics was observed after the durability test under the other environmental conditions (Fig. S19, SI). The stability of the stamps was observed throughout six months, and there were no observable changes. This innovative use of luminescent MOG-based materials emphasizes their effectiveness in sophisticated security applications and showcases their potential for large-scale deployment in anticounterfeiting and encryption technologies.

3.6. Detection of bilirubin

To establish an approach for bilirubin (BR) analysis, a fluorescence-based assay using the xerogel was used to detect the presence of the biomarker. An ultrasonicated dispersion of **SSICG15-MOG** in an aqueous medium with a volume of 2000 μL was employed as a template for the fluorescence-based experiment, to which 100 μL each of a variety of metal ions (Fe^{2+}, Fe^{3+}, Zn^{2+}, Ca^{2+}, Mg^{2+}, Na^{+}, K^{+}, Cd^{2+}) and biomarkers (BR, dopamine, creatinine, uric acid, urea, glucose, alanine, glycine, leucine, lysine, hemin, and TPYP ((5,10,15,20-tetra(4-pyridyl)porphyrin) were added. Among all the analytes, the fluorescence intensity of **SSICG15-MOG** was completely suppressed only in the presence of BR (Fig. 5a and Fig. S21a–s, SI). An anti-interference study was also conducted to evaluate the selectivity of the material, where 100 μL BR was added to the dispersed solution of the xerogel in the presence of 100 μL of each analyte individually, and their competitive fluorescence spectra were recorded (Fig. 5b and Fig. S22a–s, SI). Fluorescence quenching observations were quantified using the Stern–Volmer equation[70] (eqn (S2), SI). According to the results of the *S–V* plot analysis, which was conducted with an excellent correlation coefficient (R^2 = 0.9974), the K_{SV} value for BR was found to be 1.98×10^5 M^{-1} accordingly (Fig. S23a). The limit of detection was found to be 20 nM and established using eqn (S3) (Fig. S23b, SI). The xerogel demonstrates a high K_{SV} value and an exceptionally low detection limit, signifying good selectivity for BR. The 3D K_{SV} bar chart for all analytes indicates that stringent quenching was exclusively detected for BR, demonstrating strong selectivity for the corresponding analytes (Fig. 5c). To further elucidate comparable characteristics, a fluorescence quenching investigation for **SSICG15** was conducted. Among the analytes, **SSICG15** exhibited significant fluorescence quenching solely in the presence of BR (Fig. S24a and Fig. S26a–s, SI). Selectivity was confirmed using competitive fluorescence experiments, in which 100 μL of BR was added to the MOF dispersion along with 100 μL of each analyte individually, exhibiting a selective quenching effect by BR (Fig. S27a–s, SI). The Stern–Volmer analysis revealed a high correlation coefficient (R^2 = 0.995), a K_{SV} value of 4.7×10^4 M^{-1}, and a detection limit of 26.5 nM (Fig S24b and S25, SI). These findings highlight the significant selectivity and sensitivity of **SSICG15** towards BR, consistent with the behavior observed for **SSICG15-MOG**. The observed results for BR detection demonstrate commendable efficiency comparable to other reported benchmark materials (Table S5, SI).

3.7. Mechanism of bilirubin detection

The sensing mechanism behind high selectivity was investigated *via* theoretical and experimental studies. The most common phenomena, such as static and dynamic quenching, competitive absorption, and structural destruction, may cause this turn-off mechanism. The almost similar PXRD pattern and superimposable FTIR spectral data before and after the sensing experiment reveal the retention of the structural integrity of the whole framework (Fig. S28 and S29, SI). Hence, selective turn-off sensing *via* framework destruction was ruled out. On the other hand, the K_{SV} graph of bilirubin (BR) sensing suggests that linearity is maintained throughout the detection process from lower to higher concentrations of BR. This indicates that the static or dynamic process may contribute differently to this sensing mechanism. The possibility of competitive adsorption phenomena may play a role in this quenching mechanism. The UV-vis spectral data of all analytes were examined along with the absorbance band of the xerogel. No apparent overlapping zone was observed between the absorbance band of the xerogel and bilirubin (BR), which excluded the possibility of sensing *via* the inner filter effect (IFE)[71] or competitive absorption (Fig. S32, SI). To further investigate whether static or dynamic quenching was involved in this turn-off mechanism, time-correlated single-photon counting (TCSPC) was performed. A notable change in the mean lifespan was detected using eqn (S4) and (S5) (SI) for **SSICG15** and **SSICG15-MOG**. Prior to the addition of BR, the lifetime was 14 ns for both the MOF and MOG, which subsequently fell to 6.39 ns for **SSICG15** and 7 ns for **SSICG15-MOG** following the addition of BR (Fig. 5e and Fig. S33a, Tables S6, S7, SI).

DFT calculations of ground state and excited state energy for the ligand (H_2L) and BR ruled out the possibility of static quenching. As a primary effect, photoinduced electron transfer (PET) and fluorescence resonance energy transfer (FRET) may contribute to this selective sensing process.[71] The PET mechanism involves the transfer of electrons from the lowest unoccupied molecular orbital (LUMO) of the probe to the LUMO of the analyte. Hence, the probe's LUMO energy level needs to be greater than BR's LUMO. **SSICG15-MOG** was synthesized by combining Zn^{2+} and H_2L, and the emission spectrum of MOG was solely responsible for the H_2L ligand. The HOMO–LUMO energy gaps of the linker and BR molecules were calculated

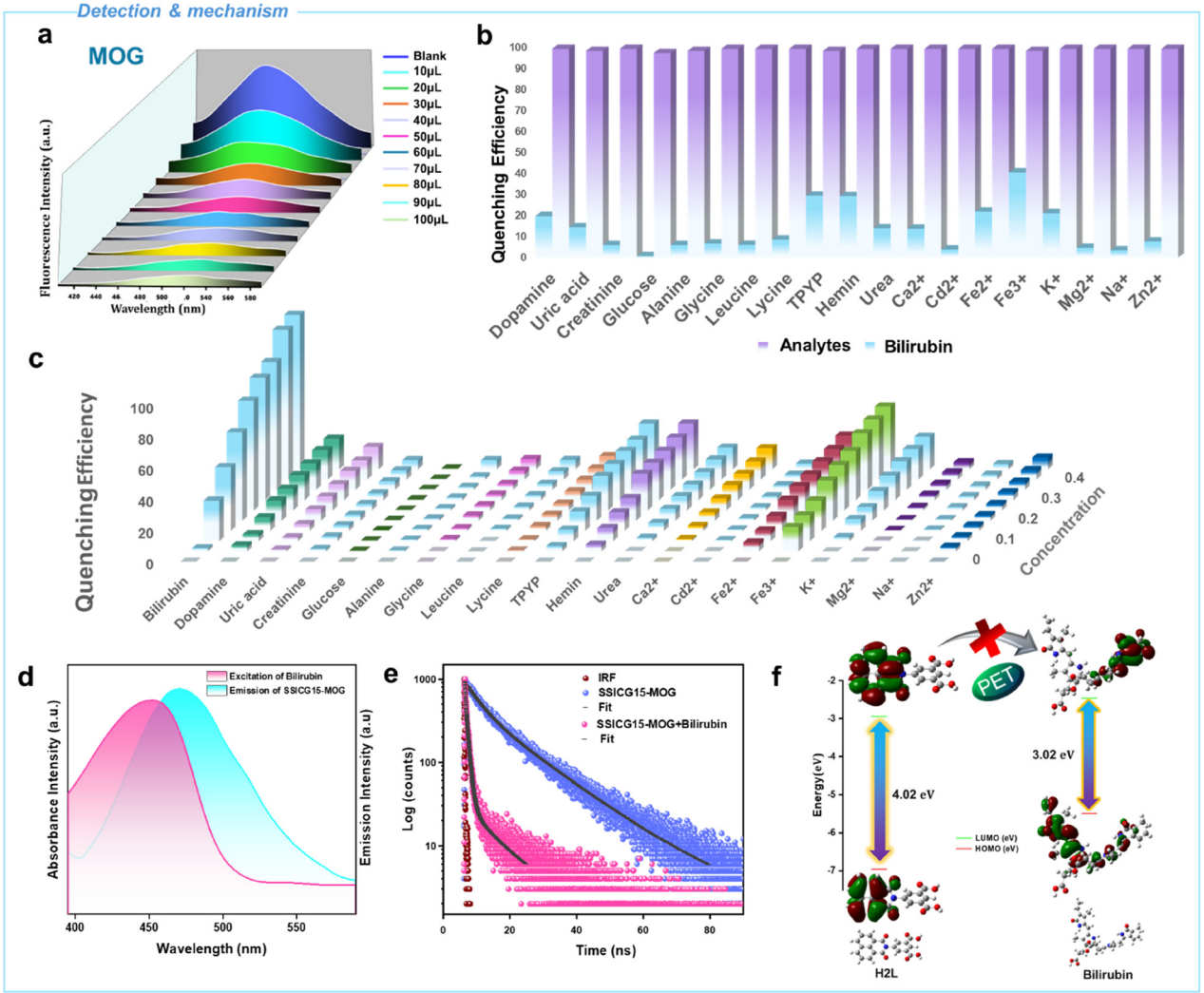

Fig. 5 (a) Fluorescence titration plot for the detection of bilirubin (BR) using the **SSICG15-MOG** suspension; (b) 3D plot of the anti-interference test in the presence of difference analytes; (c) 3D *S*–*V* diagram for all analytes; (d) FRET overlap between the excitation of BR and the emission of the xerogel; (e) time-correlated single-photon counting spectra of **SSICG15-MOG** before and after the addition of BR; and (f) ground state and excited state energies calculated for the ligand (H_2L) and BR.

using density functional theory (DFT) at the B3LYP/6-311+G(d,p) level to check the possibility of the electron transfer process. The LUMO (−2.9397 eV) of the linker has a lower energy than the LUMO (−2.466 eV) of the BR molecule (Fig. 5f).[72] This restricts the electron transfer process, and the possibility of PET phenomena becomes intricate. Following Förster's energy transfer (ET) theory, the effectiveness of FRET is determined by the degree of overlap between the fluorescence emission spectrum of the energy donor and the absorption spectrum of the receptor. The emission of the MOG donor significantly overlaps with the absorption of the BR acceptor. The extent of overlap is measured by the overlap integral ($J(\lambda)$), calculated using eqn (1):[73,74]

$$J(\lambda) = \int_0^{\infty} F_D(\lambda)\varepsilon_A(\lambda)\lambda^4 dy \quad (1)$$

$F_D(\lambda)$ represents the adjusted fluorescence intensity of the donor within the interval λ to $\lambda + \Delta\lambda$, with the overall intensity normalized to one, whereas $\varepsilon_A(\lambda)$ denotes the extinction coefficient of the acceptor at λ in M^{-1} cm^{-1}. For a FRET process to be extinguished, the distance between the energy donor and receptor should be less than 10 nm (Fig. 5d and Fig. S33b). The energy transfer efficiency is denoted by E, where τ_{D-A} and τ_D represent the average fluorescence lifetime of the xerogel without and with BR. A 50% energy transfer efficiency was calculated using eqn (2):[75]

$$E = 1 - \frac{\tau_{DA}}{\tau_A} \quad (2)$$

The Förster distance denoted by R_0 was calculated using eqn (3) between the MOG and BR. The distance R_0 was found to be 5.5 nm, which lies in the range of FRET overlap.

$$R_0 = 0.211\left[k^2 n^{-4} \Phi J(\lambda)\right]^{\frac{1}{6}} \quad (3)$$

k^2 is the orientation factor of the donor and acceptor transition dipoles, which is assumed to be 2/3. Φ is the quantum yield of the donor, which was found to be 10%. The medium's refractive index

is denoted by n (1.33 for water). $J(\lambda)$ is the integral of the overlap values, which is 3.712×10^{10} nm^4 M^{-1} cm^{-1} and was calculated using Fluortools software.[75] These findings firmly identify Förster resonance energy transfer (FRET) as the primary mechanism responsible for the quenching phenomenon, highlighting its essential significance in the observed luminescent behaviour.

4. Conclusion

This study demonstrates the dual use and adaptability of an alternate zinc cluster based MOF and its analogous MOG equivalent, made up of zinc nitrate and a naphthalimide ligand (H_2L). Unique trinuclear and tetranuclear zinc clusters were identified by structural analysis, which helped to explain the coordination framework and made it easier to simulate the MOG structure using molecular dynamics. PXRD confirmation of the xerogel's crystallinity further confirmed long-range ordering and structural similarities to the MOF. The remarkable photoluminescent characteristics of both materials enabled their use in cutting-edge anti-counterfeiting technologies *via* the creation of luminescent inks and QR code stamping. Both the MOG and MOF showed excellent sensitivity and selectivity in bilirubin (BR) detection with a high K_{SV} of 1.98×10^5 M^{-1} and 4.7×10^4 M^{-1}, and a low detection limit of 20 nM and 26.5 nM, making them a viable option for biological applications, especially in the diagnosis of jaundice. The FRET process was found to be largely responsible for the observed fluorescence quenching behavior, which improved our comprehension of their photophysical interactions. This study demonstrates structural similarities between **SSICG15-MOG** and **SSICG15** as analogous materials with significant potential for critical applications in materials design, healthcare, and security encryption.

Author contributions

J. R., S. M., and D. S. designed the project. J. R. synthesised and characterised all the materials. J. R. and S. M. conducted the density functional theory (DFT) calculations. P. M. optimized the molecular dynamics (MD) simulations. The manuscript was authored by J. R., S. M., P. M. and D. S. All authors have approved the final version of the manuscript.

Conflicts of interest

There are no conflicts to declare.

Data availability

All the data supporting this article have been included in the main manuscript as well as the supplementary informatio (SI). The supplementary information contains PXRD, IR, BET, SCXRD, UV, PL, NMR, rheology, and ESI-MS data. See DOI: **https://doi.org/10.1039/d5tc01391g**.

CCDC 2375051 contains the supplementary crystallographic data for this paper.[76]

Acknowledgements

J. R. and S. M. express their gratitude to the Indian Institute of Technology Patna for providing the necessary resources. SAIF IIT Patna is acknowledged for providing access to the single crystal XRD, TGA, and ESI-MS instrumental facilities. D. S. acknowledges the Council of Scientific and Industrial Research (CSIR) of the Government of India for providing a research grant under sanction CSIR-01(3057)/21/EMR-II.

References

1 R. Freund, O. Zaremba, G. Arnauts, R. Ameloot, G. Skorupskii, M. Dincă, A. Bavykina, J. Gascon, A. Ejsmont, J. Goscianska, M. Kalmutzki, U. Lächelt, E. Ploetz, C. S. Diercks and S. Wuttke, *Angew. Chem., Int. Ed.*, 2021, **60**, 23975–24001.
2 G. Zhong, D. Liu and J. Zhang, *J. Mater. Chem. A*, 2018, **6**, 1887–1899.
3 H. Wu, J. Zheng, A.-L. Kjøniksen, W. Wang, Y. Zhang and J. Ma, *Adv. Mater.*, 2019, **31**, 1806204.
4 Y.-X. Tan, T.-T. Ying, X.-W. Fan, Y.-L. Huang, M.-Y. Wan, Q.-L. Li, F.-X. Wang and M.-N. Wang, *Mater. Adv.*, 2023, **4**, 4755–4760.
5 S. Ghara, S. Bera and P. Dastidar, *ACS Appl. Bio Mater.*, 2023, **6**, 4749–4763.
6 E. Saha, H. Jungi, S. Dabas, A. Mathew, R. Kuniyil, S. Subramanian and J. Mitra, *Inorg. Chem.*, 2023, **62**, 14959–14970.
7 P. K. Giri, V. Parihar, S. Kumar and C. M. Nagaraja, *ACS Appl. Nano Mater.*, 2024, **7**, 15488–15497.
8 R. Sahoo, B. Pramanik, S. Mondal and M. C. Das, *Small*, 2024, **20**, 2309281.
9 Y. Lu and Z. Ke, *Small*, 2024, **20**, 2403767.
10 R.-R. Liang, Z. Han, P. Cai, Y. Yang, J. Rushlow, Z. Liu, K.-Y. Wang and H.-C. Zhou, *J. Am. Chem. Soc.*, 2024, **146**, 14174–14181.
11 R. Patra, S. Sahoo, Deepanshu, T. Rom, A. K. Paul and D. Sarma, *Inorg. Chem.*, 2024, **63**, 23396–23410.
12 R. Sahoo, S. Mondal, S. Chand, A. K. Manna and M. C. Das, *Small*, 2023, **19**, 2304581.
13 V. Singh, A. D. Dwivedi and R. Pandey, *Langmuir*, 2024, **40**, 5121–5136.
14 R. Goswami, N. Seal, S. R. Dash, A. Tyagi and S. Neogi, *ACS Appl. Mater. Interfaces*, 2019, **11**, 40134–40150.
15 S. Mondal, R. Sahoo and M. C. Das, *Small*, 2025, **21**, 2409095.
16 G.-L. Yang, X.-L. Jiang, H. Xu and B. Zhao, *Small*, 2021, **17**, 2005327.
17 M. H. Zahir, A. Helal and A. S. Hakeem, *Energy Fuels*, 2021, **35**, 10199–10209.

18 S. Gaber, A. K. Mohammed, B. H. Javaregowda, J. I. Martínez, P. P. Sánchez, F. Gándara, K. Krishnamoorthy and D. Shetty, *Angew. Chem., Int. Ed.*, 2024, **63**, e202409256.
19 S. Bera, A. Dutta and P. Dastidar, *Chem. – Asian J.*, 2024, **19**, e202400419.
20 Q. Ke, K. Jiang, H. Li, L. Zhang and B. Chen, *ACS Nano*, 2024, **18**, 21911–21924.
21 X.-G. Wang, L. Xu, M.-J. Li and X.-Z. Zhang, *Angew. Chem., Int. Ed.*, 2020, **59**, 18078–18086.
22 B. Zhang, Y. Gan, C. Liu, Q. He, J. Chen, J. Li, Y. You, W. Fan, Y. Wang and G. Bai, *Dalton Trans.*, 2024, **53**, 8626–8632.
23 Y. Yang, Y. Li, Y. Chen, Z. Wang, Z. He, J. He and H. Zhao, *ACS Appl. Mater. Interfaces*, 2022, **14**, 21330–21339.
24 J. A. Mason, M. Veenstra and J. R. Long, *Chem. Sci.*, 2014, **5**, 32–51.
25 B. Li, H.-M. Wen, W. Zhou and B. Chen, *J. Phys. Chem. Lett.*, 2014, **5**, 3468–3479.
26 D. Yang and B. C. Gates, *ACS Catal.*, 2019, **9**, 1779–1798.
27 W. P. Lustig, S. Mukherjee, N. D. Rudd, A. V. Desai, J. Li and S. K. Ghosh, *Chem. Soc. Rev.*, 2017, **46**, 3242–3285.
28 P. Deria, J. E. Mondloch, O. Karagiaridi, W. Bury, J. T. Hupp and O. K. Farha, *Chem. Soc. Rev.*, 2014, **43**, 5896–5912.
29 O. Yaghi, H. Li and T. Groy, *J. Am. Chem. Soc.*, 1996, **118**, 9096–9101.
30 A. H. Alawadhi, S. Chheda, G. D. Stroscio, Z. Rong, D. Kurandina, H. L. Nguyen, N. Rampal, Z. Zheng, L. Gagliardi and O. M. Yaghi, *J. Am. Chem. Soc.*, 2024, **146**, 2160–2166.
31 N. Alam, S. Mondal and D. Sarma, *Coord. Chem. Rev.*, 2024, **504**, 215673.
32 A. Y.-Y. Tam and V. W.-W. Yam, *Chem. Soc. Rev.*, 2013, **42**, 1540–1567.
33 S. Mondal, N. Alam and D. Sarma, *ACS Appl. Eng. Mater.*, 2024, **2**, 1467–1482.
34 D. Saha, D. Talukdar, I. Pal, S. Majumdar, G. Lepcha, S. Sadhu, S. K. Yatirajula, G. Das and B. Dey, *Langmuir*, 2024, **40**, 19816–19829.
35 S. Mondal, R. Patra, J. Ray and D. Sarma, *ACS Appl. Nano Mater.*, 2024, **7**, 26765–26776.
36 T. Feldner, M. Häring, S. Saha, J. Esquena, R. Banerjee and D. D. Díaz, *Chem. Mater.*, 2016, **28**, 3210–3217.
37 G. Picci, C. Caltagirone, A. Garau, V. Lippolis, J. Milia and J. W. Steed, *Coord. Chem. Rev.*, 2023, **492**, 215225.
38 M.-O. M. Piepenbrock, G. O. Lloyd, N. Clarke and J. W. Steed, *Chem. Rev.*, 2010, **110**, 1960–2004.
39 J. Zhang and C.-Y. Su, *Coord. Chem. Rev.*, 2013, **257**, 1373–1408.
40 J. Fu, Z. He, E. Schott, H. Fei, M. Tu and Y. N. Wu, *Small*, 2023, **19**, 2206718.
41 J. Baek, B. Rungtaweevoranit, X. Pei, M. Park, S. C. Fakra, Y.-S. Liu, R. Matheu, S. A. Alshmimri, S. Alshehri, C. A. Trickett, G. A. Somorjai and O. M. Yaghi, *J. Am. Chem. Soc.*, 2018, **140**, 18208–18216.
42 B. An, Z. Li, Y. Song, J. Zhang, L. Zeng, C. Wang and W. Lin, *Nat. Catal.*, 2019, **2**, 709–717.
43 P. Mondal, Z. Neuschuler, D. Mandal, R. E. Hernandez and S. M. Cohen, *Angew. Chem., Int. Ed.*, 2024, **63**, e202317062.
44 S. Bera, H. K. Datta and P. Dastidar, *ACS Appl. Mater. Interfaces*, 2022, **15**, 25098–25109.
45 B. C. Roy, V. R. Ramlal, D. Basak, S. Basak, S. Roy, S. Ghosh and T. Singha Mahapatra, *Inorg. Chem.*, 2024, **63**, 23044–23056.
46 S. A. Roget, Z. A. Piskulich, W. H. Thompson and M. D. Fayer, *J. Am. Chem. Soc.*, 2021, **143**, 14855–14868.
47 C. Zhang, Q. Yin, S. Ge, J. Qi, Q. Han, W. Gao, Y. Wang, M. Zhang and J. Dong, *Mater. Res. Bull.*, 2024, **176**, 112801.
48 H. Suo, Q. Zhu, X. Zhang, B. Chen, J. Chen and F. Wang, *Mater. Today Phys.*, 2021, **21**, 100520.
49 W. Ren, G. Lin, C. Clarke, J. Zhou and D. Jin, *Adv. Mater.*, 2020, **32**, 1901430.
50 A. Abdollahi, H. Roghani-Mamaqani, B. Razavi and M. Salami-Kalajahi, *ACS Nano*, 2020, **14**, 14417–14492.
51 H.-M. Yang, G.-P. Yang and Y.-Y. Wang, *J. Mater. Chem. C*, 2024, **12**, 6831–6840.
52 M. C. Heffern, L. M. Matosziuk and T. J. Meade, *Chem. Rev.*, 2014, **114**, 4496–4539.
53 S. Borse, Z. V. P. Murthy, T.-J. Park and S. K. Kailasa, *ACS Appl. Nano Mater.*, 2021, **4**, 11949–11959.
54 R. S. Tabatabaee, H. Golmohammadi and S. H. Ahmadi, *ACS Sens.*, 2019, **4**, 1063–1071.
55 W. Yang, J. Xia, G. Zhou, D. Jiang and Q. Li, *RSC Adv.*, 2018, **8**, 17854–17859.
56 E. Ahmmed, A. Mondal, A. Sarkar, S. Chakraborty, S. Lohar, N. C. Saha, K. Dhara and P. Chattopadhyay, *ACS Appl. Bio Mater.*, 2020, **3**, 4074–4080.
57 M. A. Chanu, S. Mondal, N. Zehra, A. S. Tanwar and P. K. Iyer, *ACS Appl. Polym. Mater.*, 2022, **4**, 3491–3497.
58 Z. Lu, Z. Xiao, J. Wang, Z. Zhao, J. Huang, J. Cui, Y. Mei and G. Huang, *Adv. Mater. Technol.*, 2024, **9**, 2400344.
59 S. Nandi and S. Biswas, *Dalton Trans.*, 2019, **48**, 9266–9275.
60 Y. Zhao, X.-G. Yang, X.-M. Lu, C.-D. Yang, N.-N. Fan, Z.-T. Yang, L.-Y. Wang and L.-F. Ma, *Inorg. Chem.*, 2019, **58**, 6215–6221.
61 D. Singh and J. B. Baruah, *Tetrahedron Lett.*, 2008, **49**, 4374–4377.
62 A. Pratasouskaya, V. Bon, A. Müller, S. Kaskel and F. Auras, *J. Am. Chem. Soc.*, 2024, **146**, 29491–29495.
63 W. Chen, S. Zhang, T. Su, Y. Nie, J. He, P. Xue and J. Jia, *Langmuir*, 2023, **39**, 12384–12391.
64 P. Mondal, B. K. Brahma, D. K. Vali, J. Ray, J. V. Kasu, A. Gangopadhyay, S. Laha and U. Adhikari, *Chem. – Eur. J.*, 2024, e202400587.
65 L. Cao, P. Wang, X. Miao, H. Duan, H. Wang, Y. Dong, R. Ma, B. Zhang, B. Wu and X. Li, *Inorg. Chem.*, 2019, **58**, 6268–6275.
66 P. Wang, X. Miao, Y. Meng, Q. Wang, J. Wang, H. Duan, Y. Li, C. Li, J. Liu and L. Cao, *ACS Appl. Mater. Interfaces*, 2020, **12**, 22630–22639.
67 S. K. Shevell, *The science of color*, 2003, pp. 149–190.
68 C. Gogoi and S. Biswas, *Cryst. Growth Des.*, 2021, **21**, 2680–2689.
69 J. Massue, L. Diarra, I. Georgoulis, A. Fihey, F. Robin-le Guen, G. Ulrich, M. Fakis and S. Achelle, *ChemPhotoChem*, 2023, **7**, e202300085.

70 R. Goswami, S. C. Mandal, N. Seal, B. Pathak and S. Neogi, *J. Mater. Chem. A*, 2019, **7**, 19471–19484.
71 S. Sahoo, S. Mondal and D. Sarma, *Coord. Chem. Rev.*, 2022, **470**, 214707.
72 J. Qin, B. Ma, X.-F. Liu, H.-L. Lu, X.-Y. Dong, S.-Q. Zang and H. Hou, *J. Mater. Chem. A*, 2015, **3**, 12690–12697.
73 Z. Liang, M. Kang, G. F. Payne, X. Wang and R. Sun, *ACS Appl. Mater. Interfaces*, 2016, **8**, 17478–17488.
74 S. S. Nagarkar, B. Joarder, A. K. Chaudhari, S. Mukherjee and S. K. Ghosh, *Angew. Chem., Int. Ed.*, 2013, **52**, 2881–2885.
75 L. Mishra, R. K. Behera, A. Panigrahi and M. K. Sarangi, *J. Phys. Chem. Lett.*, 2022, **13**, 4357–4364.
76 J. Ray, S. Mondal, P. Mondal and D. Sarma, CCDC 2375051: Experimental Crystal Structure Determination, 2025, DOI: **10.5517/ccdc.csd.cc2kqfk9**.